A cross–nearest neighbor/Monte Carlo algorithm for single molecule localization microscopy defines interactions between p53, Mdm2, and MEG3

Nicholas C. Bauer[1], Anli Yang[2†§], Xin Wang[2†‖], Yunli Zhou[2], Anne Klibanski[2‡¶], Roy J. Soberman[1*‡]

[1]Division of Nephrology, Department of Medicine, Massachusetts General Hospital and Harvard Medical School, Charlestown, Massachusetts, United States

[2]Neuroendocrine Unit, Department of Medicine, Massachusetts General Hospital and Harvard Medical School, Boston, Massachusetts, United States

[†] These authors contributed equally to the work

[‡] These authors contributed equally to the work

[§] Current affiliation: Department of Histology and Embryology, Guangdong Pharmaceutical University, Guangzhou, Guangdong, China

[‖] Current affiliation: Department of Breast Oncology, Sun Yat-sen University Cancer Center, Guangzhou, Guangdong, China

[¶] Current affiliation: Mass General Brigham, Boston, Massachusetts, United States

*Corresponding author: Roy Soberman

E-mail: soberman@helix.mgh.harvard.edu

Running title: Detecting p53 interactions in localization microscopy data

Keywords: p53, mouse double minute 2 homolog (Mdm2), long noncoding RNA (long ncRNA, lncRNA), microscopy, computational biology, image analysis, single molecule localization microscopy (SMLM), stochastic optical reconstruction microscopy (STORM)

Abstract

The functions of long noncoding (lnc)RNAs such as MEG3 are defined by their interactions with other RNAs and proteins. These interactions, in turn, are shaped by their subcellular localization and temporal context. Therefore, it is important to be able to analyze the relationships of lncRNAs while preserving cellular architecture. The ability of MEG3 to suppress cell proliferation led to its recognition as a tumor suppressor. MEG3 has been proposed to activate p53 by disrupting the interaction of p53 with Mdm2. To test this mechanism in the native cellular context, we employed two-color direct stochastic optical reconstruction microscopy (dSTORM), a single-molecule localization microscopy (SMLM) technique to detect and quantify the localizations of p53, Mdm2, and MEG3 in U2OS cells. We developed a new cross–nearest neighbor/Monte Carlo algorithm to quantify the association of these molecules. Proof of concept for our method was obtained by examining the binding between MEG3 and p53, and Mdm2 and p53. In contrast to previous models, our data support a model in which MEG3 modulates p53 independently of the interaction with Mdm2.

Introduction

Long noncoding RNAs (lncRNAs) function in cell-type and subcellular localization–dependent contexts; how they do so is poorly understood. The human *MEG3* lncRNA gene is located on chromosome 14q32 and belongs to the conserved, imprinted *DLK1-MEG3* locus (1,2). MEG3 transcripts are detected in a wide range of normal tissues, including endocrine tissues, brain, gonads, and placenta (1). MEG3 modulates the activity of multiple miRNAs; for example, MEG3 functions as a decoy for miR-138 (3) allowing it to regulate the generation of IL-1β in macrophages in models of host defense. MEG3 has also been reported to directly interact with DNA to modulate the transcription of TGF-β pathway genes (4).

Based on the observation that *MEG3* expression is lost in clinically non-functioning pituitary adenomas, we identified *MEG3* as a tumor suppressor (1,5-7). Compared to normal tissue, MEG3 expression is also significantly reduced or absent in meningiomas (8), epithelial ovarian cancer (9), and squamous cell carcinoma of the tongue (10); supporting its role as a tumor suppressor. This function was further supported by studies of tumor xenograft growth in nude mice (11,12). Several studies demonstrated that MEG3 expression causes an increase in cellular tumor antigen p53 (p53, UniprotKB P04637) levels and selectively activates p53 target gene expression (11,13-16), suggesting that MEG3 exerts its cellular functions via p53. However, how the MEG3 lncRNA activates p53 remains elusive. Our previous work indicated that MEG3 functions via activation of tumor suppressor p53 (16). p53 coordinates a transcription program to stall the cell cycle, promote DNA repair, and initiate senescence or apoptosis (17). The primary modulators of p53 activity are the E3 ubiquitin-protein ligase Mdm2 (Mdm2, UniprotKB Q00997) and its heterodimer partner protein Mdm4 (Mdm4, UniprotKB O1515) which constitutively polyubiquitinate p53 for proteasomal degradation, maintaining p53 at low levels (18-20). Thus, modulating the p53–Mdm2/4 interaction is a critical point of regulation for p53 activity. Signal-dependent post-translational modification of p53, including phosphorylation and acetylation, can block Mdm2/4 from binding to p53 and prevent its degradation (21). Stabilization of p53 may also be achieved through interaction with other proteins such as peptidyl-prolyl cis-trans isomerase NIMA-interacting 1 (Pin1) (22,23). It has been shown that MEG3 and p53 can be pulled down in one complex by immunoprecipitation (24,25). Therefore, one possible mechanism for p53 activation by MEG3 is disrupting the p53–Mdm2/4 interaction.

Identifying molecular associations within the spatial context of the cell is necessary to fully define the behavior of MEG3. Single molecule localization microscopy (SMLM) is exceptionally well positioned to provide this information. SMLM is unique from other microscopy approaches in that it provides high-accuracy coordinates of the positions of fluorophores rather than an image (although an image may be reconstructed from

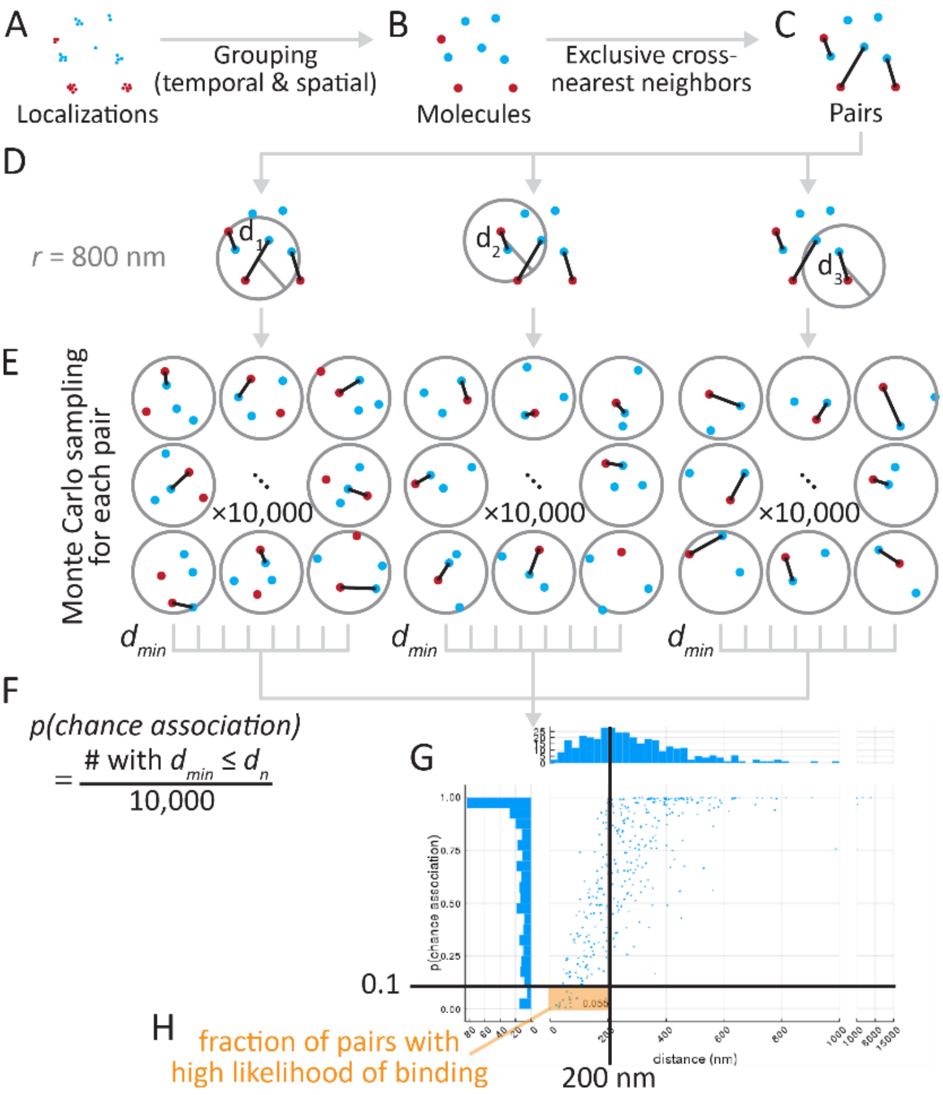
A
Localizations
Grouping
(temporal & spatial)
B
Molecules
Exclusive cross-
nearest neighbors
C
Pairs
D
r = 800 nm
d1
d2
d3
E
Monte Carlo sampling
for each pair
×10,000
×10,000
×10,000
dmin
dmin
dmin
F
p(chance association)
= # with dmin ≤ dn / 10,000
G
1.00
0.75
0.50
0.25
0.00
p(chance association)
0.1
0.055
0
200
400
600
800
1000
distance (nm)
H
fraction of pairs with
high likelihood of binding
200 nm

Figure 1. Cross–nearest neighbor/Monte Carlo method to estimate the fraction of molecules bound. Scattered localizations (A) were grouped over time and space to into “molecules” which have a position that is the average of their component localizations (B; see Figure S5). These molecules were exclusively paired to their cross–nearest neighbors (C). For each pair (D), 10,000 permutations of the molecules within radius *r* (800 nm) of the centroid of the pair were generated and the closest intermolecular distance was measured (E). The fraction of events less than the pair’s distance was the probability of chance association (*p(chance association)*) (F). These values were accumulated across the whole cell (plotted in G), and the fraction of pairs with a probability of chance association < 0.1 and within a physically possible binding distance (< 200 nm), the fraction bound, was calculated (H).

these localizations). As such, SMLM data must be analyzed with very different methods from traditional microscopy data, which are still under active development (26). The first techniques applied traditional fluorescence image analysis approaches to the reconstructed images, although much of the unique information obtained by SMLM is lost this way. More promising approaches have looked at cluster-based and tessellation-based analyses (27,28), enabling the examination of supramolecular assemblies. However, there has been little work done towards using SMLM data to measure single molecular interactions.

To fully understand the interactions of MEG3 with p53 and to test the hypothesis that MEG3 disrupts p53–Mdm2 binding, we developed a new cross–nearest neighbor/Monte Carlo algorithm to quantify the association between molecules from direct stochastic optical reconstruction microscopy (dSTORM) data. We characterized the behavior of this method *in silico* and demonstrated a proof of concept by examining the binding between MEG3 and p53, and Mdm2 and p53. Future work will build on this technique to examine the relationships of MEG3 to other cell components. In contrast to previous models, our data support a model in which MEG3 modulates p53 independently of Mdm2.

Results

Quantifying macromolecular associations by SMLM

We developed an SMLM approach that allowed us to identify potentially interacting molecules by calculating the probability that two localizations were anomalously close. We applied a Monte Carlo estimation method (Figure 1) that accounts for the local density around a candidate binding pair, partly based on a technique recently introduced for examining the association of sparse mRNAs in neurons (29).

In the first step nearby localizations were grouped into "molecules" using spatial and temporal thresholds (Figure 1A and 1B). A characteristic of dSTORM is that there is no guarantee that a single molecule will be represented by a single localization. Consider the p53 tetramer: it may be bound by up to 4 primary single-epitope antibodies, each of which may be bound by 1 or 2 secondary antibodies, each of which may have 0 to 8 fluorophores attached (despite the average being ~1 dye molecule/antibody), and each fluorophore may blink many times before permanent bleaching. A grouping algorithm is important for dSTORM data to remove such autocorrelated localizations for our downstream analysis, which here assumes that each molecule's location is independent of each other molecule.

Second, "molecules" from each channel were paired together through an exclusive cross–nearest neighbor algorithm: closest pair identified then removed, repeating until all possible pairs were made (Figure 1B and 1C). The resulting list of pairs is guaranteed to contain all detectable binding events.

The third phase of the algorithm assesses the probability that each pair is associated by chance. Within the local neighborhood (radius r = 800 nm, Figure 1D), 10,000 random permutations of the positions of the molecules within this radius were generated and the smallest paired distance measured in each iteration (Figure 1E). The fraction of permutations in which a distance d_n less than or equal to the observed distance d_{min} was recorded as the probability of chance association (*p(chance association)*) for that molecule pair (Figure 1F). These steps were repeated for each pair in each cell, and a graph of distance and probability of chance association may be generated (Figure 1G). This plot from a representative cell shows that larger distance is correlated with higher probability of chance association, with wide variability due to local density changes.

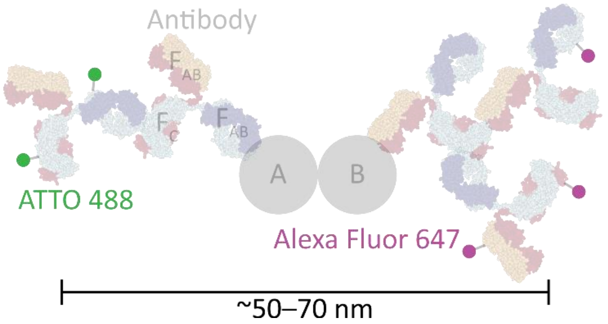

Figure 2. The physical arrangement of a bound pair and antibody stack. Typical immunofluorescence uses expensive, target-specific primary antibodies and cheap secondary antibodies conjugated to a fluorophore like ATTO 488 and Alexa Fluor 647. For orientation, one antibody is labeled for its constant domain (F_C) and two antigen binding domains (F_{AB}). The physical size and arrangement mean that ~50–70 nm may separate signal from the two fluorophores when detecting a binding interaction between proteins A and B, and multiple fluorophores can produce signal spread over tens of nanometers. Antibody graphic was created using NGL Viewer (51) from RCSB PDB 1IGT.

Finally, these pairwise measures of association were reduced into a summary value which would correlate with fraction bound. We considered pairs with a probability of chance association less than 0.1 and a distance of less than 200 nm to be bound, and used that value to generate the final output, fraction bound (Figure 1H). In this example, the average distance of the pairs in the "bound" fraction is approximately 50 nm, which corresponds well with the range expected due to the size of the antibody stacks used to detect molecules (up to ~50–70 nm between fluorophores, Figure 2). In this dataset, pairs with a large distance but a low probability of chance association were rare; most of those pairs classified as unbound were due to moderately close pairs in dense areas.

Algorithm performance improves with lower density, shorter distances

A natural limitation of our algorithm is that it strongly depends on the density of localizations and the distance between the fluorophores of an associated pair. To characterize this behavior, we simulated 30 distributions of molecules (i.e. the product of the grouping algorithm described above) for each combination of density (100, 200, 500, 1000, 2000, 5000, and 10000 molecules of each kind within a 250 μm^2 circle), percent binding (0, 1, 2, 5, 10, 20, 50, and 100%), and physical distance

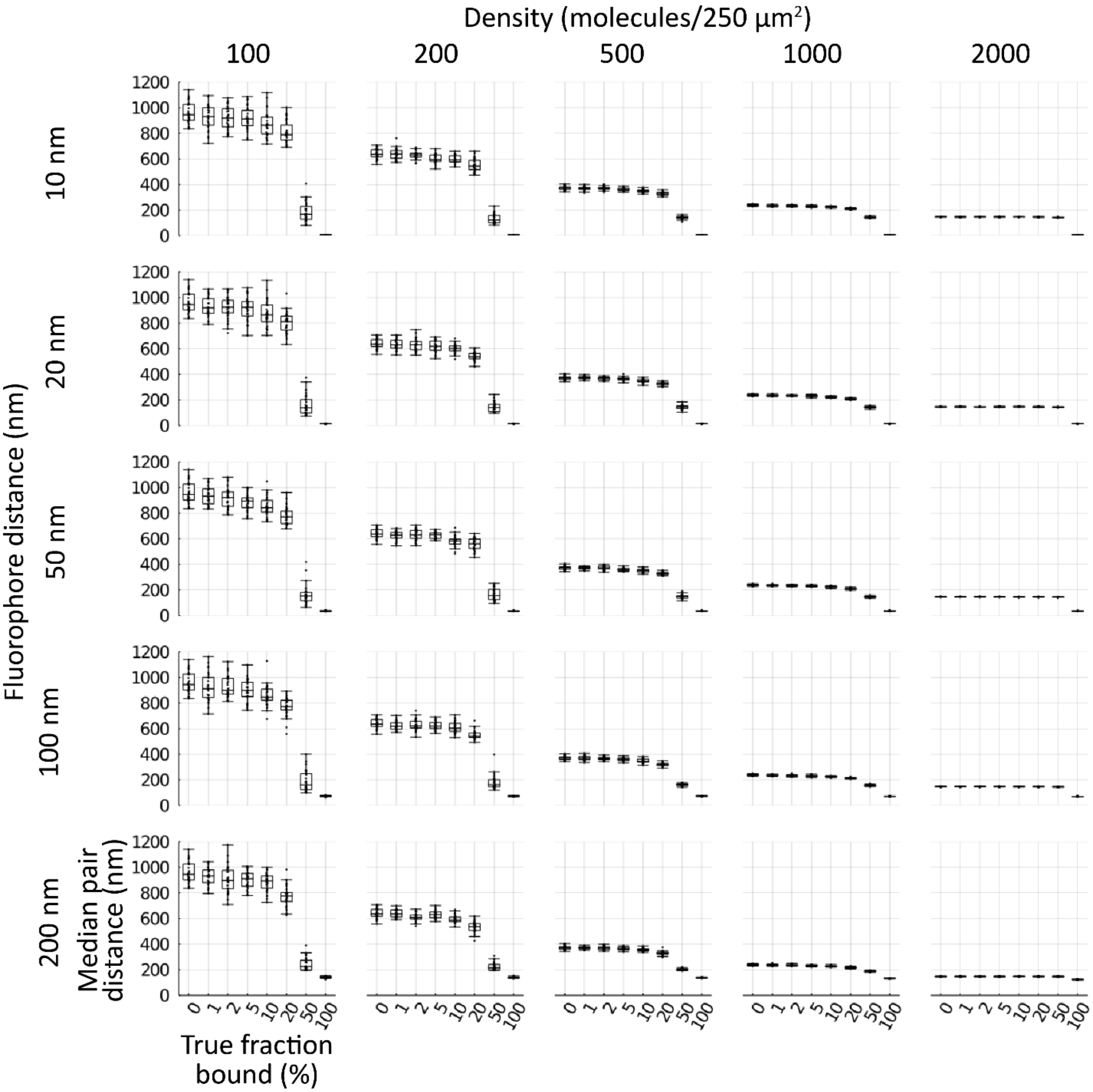

Figure 3. Density and pair distance determine median distance. Simulated cells of 100, 200, 500, 1000, 2000 molecules of each type (columns left to right) within a 250 µm^2 circle with 10, 20, 50, 100, 200 nm separation between pairs (rows top to bottom) for cells with 0, 1, 2, 5, 10, 20, 50, or 100% binding were generated (n = 30 each condition). Molecules for each simulated cell was run through the cross–nearest neighbor/Monte Carlo algorithm and median distance between pairs measured. Boxes indicate median +/- upper and lower quartile; whiskers indicate the range excluding outliers.

between fluorophores (10, 20, 50, 100, and 200 nm). Higher density naturally means that the two sets of localizations are closer together on average (Figure 3, columns from left to right), while larger binding distance inflates the value they converge to as more of the molecules are bound together (Figure 3, rows from top to bottom). The Monte Carlo component of the association algorithm adjusts for local density around a putative associated pair, but the algorithm's sensitivity is reduced by higher global density (Figure 4, columns from left to right). Larger physical distance between fluorophores in a bound pair similarly reduces sensitivity, as the pair becomes harder to distinguish from the background distribution (Figure 4, rows from top to bottom). Normalizing the fraction bound using 0% and 100%

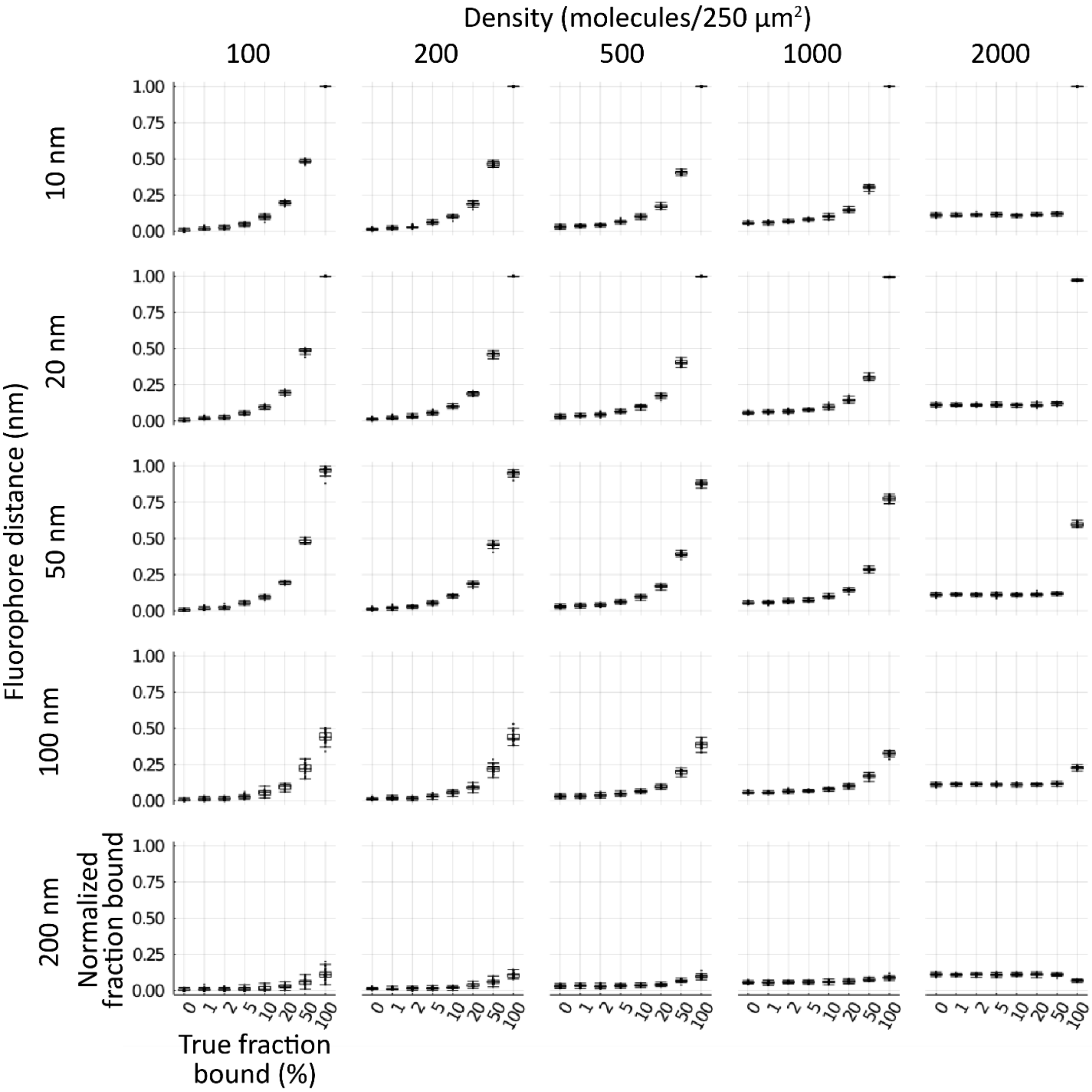

Figure 4. Density and pair distance influence fraction bound. Simulated cells of 100, 200, 500, 1000, 2000 molecules of each type (columns left to right) within a 250 µm² circle with 10, 20, 50, 100, 200 nm separation between pairs (rows top to bottom) for cells with 0, 1, 2, 5, 10, 20, 50, or 100% binding were generated (n = 30 each condition). Molecules for each simulated cell were run through the cross–nearest neighbor/Monte Carlo algorithm and median distance between pairs measured. Boxes indicate median +/- upper and lower quartile; whiskers indicate the range excluding outliers.

mean values improves the correspondence between true fraction bound and measured fraction bound, but the measured value becomes a severe underestimate of the true fraction bound at higher densities and increased pair distances (Figures S1 and S2). We applied this normalization approach to the biological data to partially correct for global density and distance between fluorophores.

MEG3–p53 interaction

We developed U2OS osteosarcoma cell clones containing a doxycycline-inducible MEG3 (U2OS-MEG3) and confirmed that MEG3 was induced 100–200-fold on doxycycline treatment as determined by qRT-PCR. We established conditions for performing dSTORM,

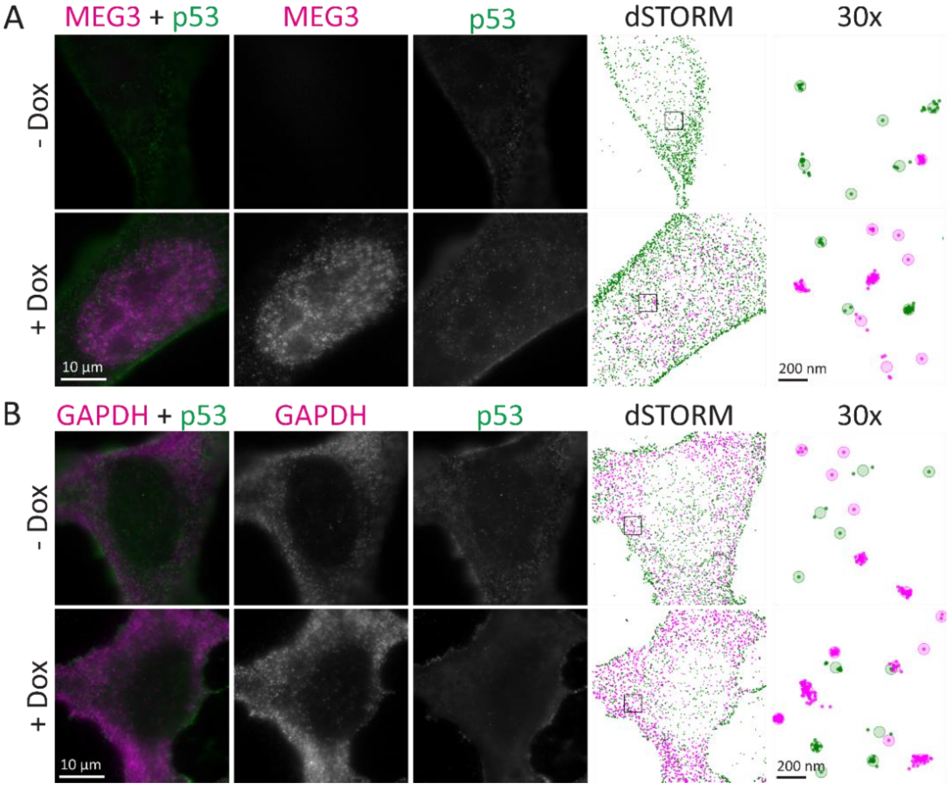

Figure 5. MEG3 localized in the nucleus of U2OS cells by epifluorescence and 2-color dSTORM. *MEG3* was induced by treatment of U2OS-MEG3 cells for 20 h with 1 µg/mL doxycycline. Cells were stained for p53 with a secondary antibody conjugated to ATTO 488 (green) and either tiled oligonucleotides recognizing MEG3 (Quasar 670, magenta, A) or GAPDH (Quasar 570, magenta, B). From left to right: Merged image; RNA channel; p53 channel; dSTORM localization map; 30x inset of dSTORM localizations in the black box, with shaded circles indicating "molecules". Scale bars are 10 µm, or 200 nm (right column).

simultaneously imaging RNA using fluorescence *in situ* hybridization (FISH) and proteins by immunofluorescence (IF). After 20 h induction with doxycycline, cells were fixed and MEG3 was labeled with a tiled probe set conjugated with Quasar 670 (magenta), and p53 was labeled with a secondary antibody conjugated to ATTO 488 (green). Cells were separately labeled for *GAPDH* mRNA with a tiled probe set conjugated with Quasar 570 (magenta) as a negative control. Large tiled widefield fluorescence images were taken (Figure S3) and ten individual cells were randomly selected from these fields for dSTORM, in each of three replicates. Representative cells are shown in Figure 5, widefield (left three columns) and dSTORM localizations and grouped molecules (right two columns, respectively). The intense fluorescence indicating MEG3 is readily apparent in the nucleus of the cells treated with doxycycline, along with p53, while very little MEG3 is apparent in untreated cells (Figure 5A). Doxycycline treatment had no apparent effect on the GAPDH mRNA distribution (Figure 5B). As seen in the detail of the molecule groups (right column), the grouping operation is slightly biased towards merging nearby clusters.

Using our cross–nearest neighbor/Monte Carlo method, we found a stark difference between MEG3 and *GAPDH* mRNA in terms of fraction bound (Figure 6A). Two-way nested ANOVA confirmed that the binding fraction was significantly larger for MEG3 than for *GAPDH* mRNA ($F = 5.487$, $p = 0.04723$, $\omega^2 = 0.06040$), but no significant effect due to doxycycline ($F = 1.740$, $p = 0.2237$, $\omega^2 = 0.009955$) and no interaction effect ($F = 2.670$, $p = 0.1409$, $\omega^2 = 0.02248$). Since only the RNA main effect was significant, a follow-up one-way nested ANOVA was performed within each RNA type. For *GAPDH* mRNA, ~0.94% of p53–*GAPDH* mRNA pairs were "bound", with virtually no change due to doxycycline (-Dox (white box): 0.82% vs. +Dox (gray box): 1.1%; $F = 0.1960$, $p = 0.6808$, $\omega^2 = -0.04127$) and little variability between cells overall, though significant inter-replicate variability was present (blue, red, orange points; $F = 3.781$, $p = 0.008795$, $\omega^2 = 0.2265$) (Figure 6A, right). There are several reasons why the method may have measured a very low level of binding between p53 and *GAPDH* mRNA. First, p53 is known to have promiscuous non-specific RNA binding capacity (30). Another contributor may be crosstalk due to the spectral overlap of the fluorophore used for *GAPDH* mRNA and p53

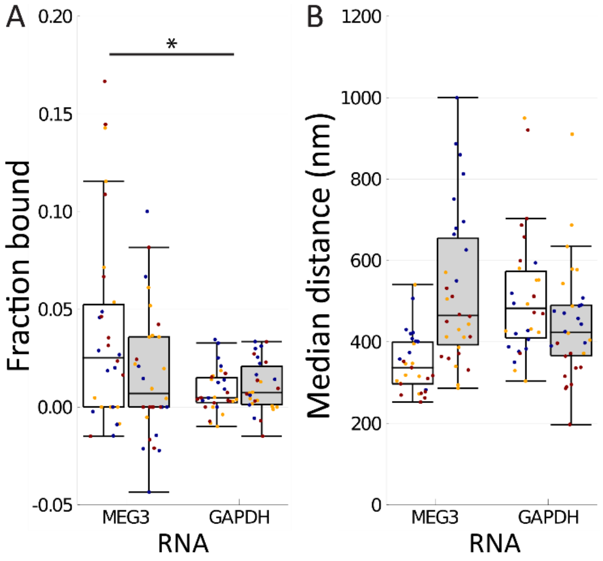

Figure 6. MEG3 associated with p53. *MEG3* was induced by treatment of U2OS-MEG3 cells for 20 h with (gray) or without (white) 1 μg/mL doxycycline. The cells were then fixed and stained for 2-color dSTORM of MEG3 and p53 (left) or *GAPDH* mRNA and p53 (right). For each condition, single molecule localizations were collected from 10 randomly chosen cells in 3 separate experiments. (A) Fraction of pairs bound, as defined by a probability of chance association < 0.1 (i.e., correction for local density) and distance < 200 nm (upper limit for binding distance, accounting for error). (B) Median distance between pairs for each cell (nm). Boxes indicate median +/- upper and lower quartile; whiskers indicate the range excluding outliers. Data points are colored by replicate. * indicates p < 0.05 by nested two-way ANOVA.

(Quasar 570 vs. ATTO 488); localizations would be associated with each other but for a technical and not biological reason.

In contrast with *GAPDH* mRNA, the median fraction of MEG3 bound to p53 as defined by this method was substantially higher at ~2.8%, and doxycycline induction did not significantly affect this amount (-Dox (white box): 3.9%, +Dox (gray box): 1.6%; F = 2.496, p = 0.1893, ω^2 = 0.040281) with wide variability but no significant difference between replicates (blue, red, orange points; F = 1.822, p = 0.1381, ω^2 = 0.07286) (Figure 6A, left). The lack of effect due to MEG3 induction suggests that the fraction of MEG3 bound to p53 inside cells remains constant across changes in MEG3 expression. For comparison, we also applied a naïve median distance approach, where we calculated the median of the pairwise distances for each cell (Figure 6B). In this simple approach, there was a high degree of overlap between MEG3 and *GAPDH* mRNA distributions (F = 0.3046, p = 0.5961, ω^2 = -0.3323), and increased inter-replicate variability is apparent with this measure (blue, red, orange points; F = 13.53, p = 2.018×10^{-13}, ω^2 = 0.5311) (Figure 6B). Thus, our cross–nearest neighbor/Monte Carlo–based approach provides a more consistent and robust measure of association over simpler approaches.

Mdm2–p53 binding maintains stable equilibrium

To determine whether MEG3 causes accumulation of p53 by disrupting the Mdm2–p53 interaction, MEG3 was induced by doxycycline in U2OS-MEG3 cells, with or without the addition of the MDM2–p53 binding inhibitor nutlin-3a. After 24 h of treatment, the cells were fixed. p53 was labeled with a secondary antibody conjugated to Alexa Fluor 647 (magenta) and Mdm2 was labeled with a secondary antibody conjugated to ATTO 488 (green). Large tiled widefield fluorescence images were taken (Figure S4) and ten individual cells were randomly selected from these fields for dSTORM analysis, in each of three replicates. Representative cells are shown in Figure 7, widefield (left three columns) and dSTORM localizations and grouped molecules (right two columns, respectively). Intense nuclear p53 fluorescence is observed on treatment with nutlin-3a, without much apparent change due to doxycycline. Mdm2 levels and localization change little between conditions. Individual cells were randomly selected from these fields for dSTORM (Figure 7).

Using our cross–nearest neighbor/Monte Carlo method, we found that nutlin-3a treatment did not cause a significant change in p53–Mdm2 binding (-Nut: 1.7%, +Nut: 1.7%; F = 0.0002317, p = 0.9882, ω^2 = -0.006422) (Figure 8A). Doxycycline treatment (MEG3 induction) did not have any significant overall effect (-Dox: 1.4%, +Dox: 1.9%; F = 2.178, p = 0.1782, ω^2 = 0.007572). There was no significant interaction effect (F = 0.08012, p = 0.7842, ω^2 = -0.005909). There was no significant inter-replicate variability (F = 0.7478, p = 0.6492, ω^2 = 0.02600). Importantly, these data suggest that MEG3 does not disrupt overall p53–Mdm2 binding. However, nutlin-3a also did not appear to disrupt p53–Mdm2 binding by this measure. These observations may in part be explained through

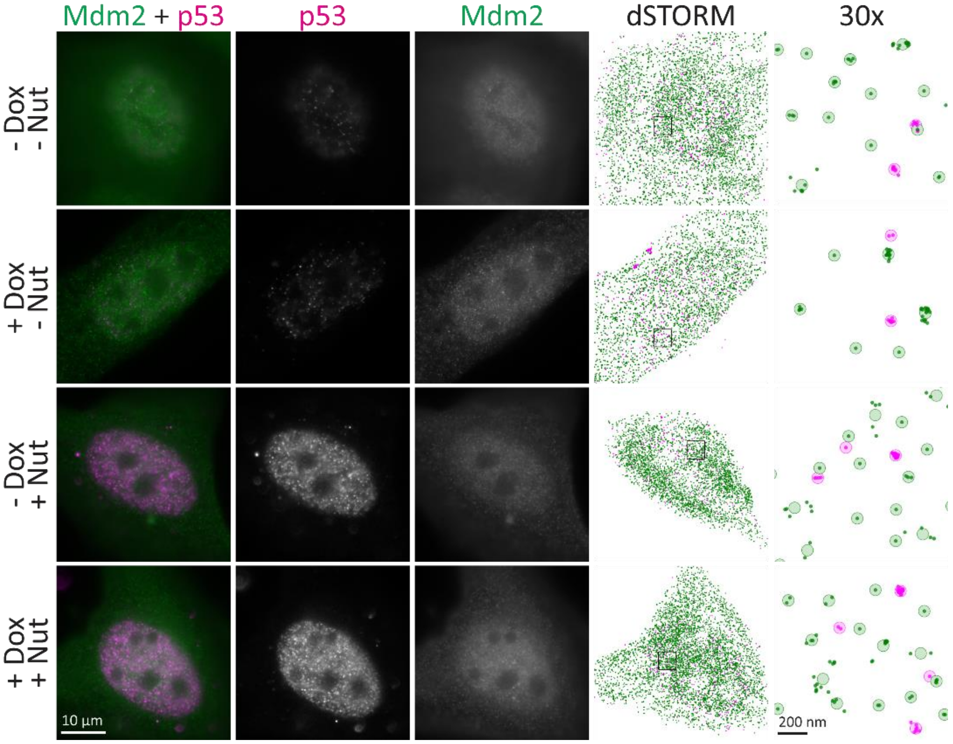

Figure 7. Nutlin-3a caused accumulation of p53 in the nucleus. *MEG3* was induced by treatment of U2OS-MEG3 cells for 20 h with 1 µg/mL doxycycline and/or 1 µg/mL nutlin-3a. Cells were stained for Mdm2 with a secondary antibody conjugated to ATTO 488 (green) and for p53 with a secondary antibody conjugated to Alexa Fluor 647 (magenta). From left to right: Merged image; RNA channel; p53 channel; dSTORM localization map; 30x inset of dSTORM localizations in the black box, with shaded circles indicating "molecules". Scale bars are 10 µm, or 200 nm (right column).

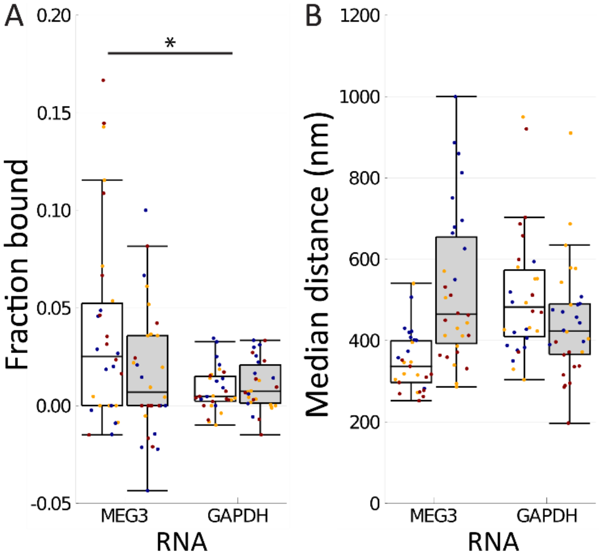

Figure 8. Nutlin-3a, but not MEG3, reduced Mdm2–p53 binding. *MEG3* was induced by treatment of U2OS-MEG3 cells for 20 h with or without 1 µg/mL doxycycline and/or 10 µM nutlin-3a. Cells were then fixed and stained for 2-color dSTORM of p53 and Mdm2. For each condition, single molecule localizations were collected from 10 randomly chosen cells in 3 separate experiments. (A) Fraction of pairs bound, as defined by a probability of chance association < 0.1 (i.e., correction for local density) and distance < 200 nm (upper limit for binding distance, accounting for error). (B) Median distance between pairs for each cell (nm). Boxes indicate median +/- upper and lower quartile; whiskers indicate the range excluding outliers. Data points are colored by replicate. * indicates $p < 0.05$ by nested two-way ANOVA.

equilibrium. For example, nutlin-3a inserts into the pocket of Mdm2 that binds to p53, preventing Mdm2 from ubiquitinating p53 and marking it for proteasomal destruction (31). Thus, levels of both proteins may accumulate until Nutlin-3a is saturated and excess Mdm2 can bind to p53. This state may be reached with a similar fraction of both proteins bound. It may also be that the interaction is relatively transient, and too close to the limit of detection for this method. For comparison, we again conducted an analysis based on naïve median distances. As with MEG3–p53 binding, we found this simple approach produced overlapping, hard-to-interpret distributions (Figure 8B).

Discussion

We developed a mathematical approach to analyzing SMLM data that we used to interrogate the interactions of MEG3. Our overall approach takes advantage of high-resolution molecule position data to calculate distances between putative binding partners, assesses the probability that the two molecules are not bound together, and thus provides an overall measure of the fraction of pairs of molecules likely bound together. Using this technique, we distinguished between non-binding pairs (*GAPDH* mRNA–p53) and binding pairs (MEG3–p53) inside cells and quantified the extent of binding between Mdm2 and p53. The mechanism of MEG3 action suggested by our experiments is different than the previously proposed mechanism in which MEG3 acts by protecting p53 from polyubiquitination by Mdm2. Moreover, the fraction of binding assessed between MEG3 and p53 indicates that there are insufficient stable interactions occurring to effectively inhibit p53–Mdm2 binding. These data suggest that MEG3 activates p53 through alternative mechanisms.

Under MEG3 induction, p53 transcription activation is selective, inducing certain p53 targets (e.g., *GDF15*) but failing to induce other p53 targets (e.g., *CDKN1A*) (16). A MEG3–p53 complex may not be competent to induce Mdm2 expression, thereby suppressing the negative feedback regulatory loop. MEG3 also interacts with the chromatin remodeler polychrome repressive complex 2 (PRC2) (32,33), which is responsible for forming heterochromatin at target sites. MEG3 targets PRC2 to certain sites via DNA triplex formation (e.g., TGF-β pathway genes) (4) and protects other sites from PRC2 activity (e.g., *MEG3* locus) (34). A recent investigation of MEG3 structure identified a pseudoknot in MEG3 critical for MEG3-dependent p53 activation, which however was not directly involved in p53 binding (35). It is also possible that MEG3 may modulate the activity of Mdm2 on p53 by forming a ternary complex with them. Similar interactions have been observed with p14^{ARF} (tumor suppressor ARF) (36), UCH-L1 (ubiquitin carboxyl-terminal hydrolase isozyme L1) (37), and the 5S RNP (38). Future work will need to address these alternative mechanisms.

There are some important challenges to the cellular SMLM-based binding analysis we have developed, and which affect SMLM analysis approaches in general. First, despite the 10–20 nm resolution of each localization, the large distance between the molecule of interest and the fluorophore limit the analytical resolution. A typical two-antibody stack can have a displacement of up to ~35 nm from the bound epitope to the conjugated fluorophore; thus, the fluorophores for a bound pair of molecules may be separated by ~50–70 nm or more (Figure 2), depending on the distance between epitopes. In addition, the antibody stack may be free to rotate and flex at the neck, adding variability in the position of the fluorophore during imaging (39). High density also impacts ability to differentiate low fraction binding, as illustrated in Figure 4. These distance issues may be addressed in part using nanobodies as secondary antibodies, which would reduce the distance to ~30–50 nm (Figure 9A). Nanobodies are small single-domain antibody fragments derived from camelids that are emerging as powerful and versatile tools for biology (40-42). Further distance reduction to ~10–30 nm and stable positioning could be achieved by introducing a fusion tag into the target gene and directly binding it with a nanobody (Figure 9B) (40). Further improvements to the algorithm may also be able to address these issues.

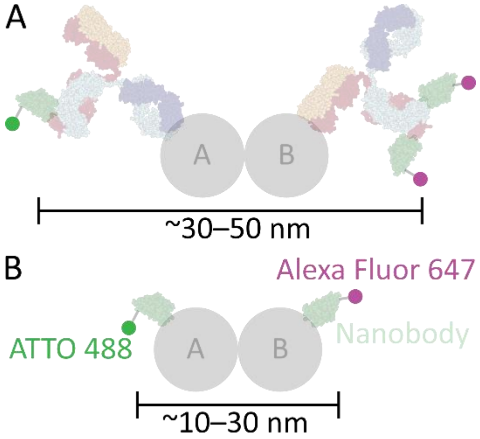

Figure 9. Nanobodies reduce distance between fluorophores for bound pairs. (A) Nanobodies (pale green) can be used in the place of secondary antibodies, reducing the distance to ~30–50 nm. (B) Nanobodies may also be used to bind directly to a target of interest, either native or via a small peptide fusion tag, reducing the distance to ~10–30 nm. Antibody and nanobody graphics were created using NGL Viewer (51) from RCSB PDB 1IGT and 5IVO, respectively.

A second set of limitations comes from the stochastic nature of SMLM. Fluorophores may blink many times, only once, or not at all (43). This phenomenon makes it difficult to distinguish between nearby molecules of the same type. We employed an aggressive grouping algorithm to address this issue, but the tradeoff is that true separate molecules may be missed. We labeled our own secondary antibodies to control the dye:antibody ratio at ~1:1 to limit multiple blinking, but the labeling creates a distribution and some antibodies will still have multiple fluorophores. Antibodies engineered to have consistent labeling stoichiometry would be an improvement. A trade-off to limiting the dye:antibody ratio is that many of the secondary antibodies will have no fluorophore, reducing labeling efficiency. SMLM techniques generally have shown a labeling efficiency of at most 60% (26). Improvements to labeling efficiency will enable rare binding interactions to be more readily detected by our method.

A third challenge for our algorithm comes from drift. Autocorrelation drift correction is standard, but it is optimal for defined structures that can be aligned from repeated blinks that occur throughout the acquisition. Singular soluble proteins, which blink only within a small window, pose a challenge for this correction method, and too few blinks overall can prevent the automatic correction from working despite apparent drift by eye. Further, this correction method cannot remove high-frequency variation in position through vibration within the microscope. Fluorescent beads may be used as a fiducial marker at the coverglass surface, but a solution is needed that would work throughout the cell. A sparsely labeled ubiquitous cellular structure, like tubulin, could serve this purpose with an appropriately engineered label. Eliminating drift effects would allow our algorithm to use smaller radii, increasing its sensitivity.

Previously, we found that MEG3 induces p53 stabilization and stimulates p53-dependent transcription activation (16). In this study, we demonstrated that MEG3 lncRNA interacts with p53 inside the cell and can be detected with a novel analytical method using dSTORM. We also demonstrated that the p53–Mdm2 interaction may not be significantly disrupted by MEG3 in cells. Taken together, these data suggest that an alternative mechanism leads to p53 activation. Finally, we believe our binding analysis provides a powerful new tool to assess macromolecular interactions in a native cellular context, with future extensions to 3-dimensional data and multi-protein complexes.

Experimental procedures

Cell lines, media, and growth conditions

The U2OS osteosarcoma cells (ATCC HTB-96) were maintained in Dulbecco's modified Eagle's medium (DMEM) (Gibco 11995065) supplemented with 10% heat-inactivated FBS (Gibco A3060502), glutamine (2 mM), penicillin (100 U/mL), and streptomycin (0.1 mg/mL) (Gibco 10378016) at 37 °C and 10% CO_2. Doxycycline (Dox; 1 µg/mL) was added to media for at least 20 h to induce expression of the transfected tetracycline-inducible *MEG3*. Nutlin-3a (Nut; 10 µM) was added to media for at least 24 h to inhibit Mdm2-mediated degradation of p53. For microscopy, $3–5\times10^4$ cells were seeded into each well of a chambered 8-well 1.5H coverglass (Ibidi 80827) and allowed to adhere overnight prior to further manipulation. Cells were tested for mycoplasma contamination every three months. U2OS-MEG3 cells were regularly authenticated by qRT-PCR and/or FISH for induction of MEG3 by doxycycline.

Plasmid construction and transfection

A modified Tet-On expression system was used to express MEG3, consisting of pBiTetO-MEG3-GFPLoxP and pCMV-rtTA3-IRESpuro. pBiTetO was constructed by replacing the CMV promoter in expression vector pCI with a tetracycline-responsive bi-directional promoter, BiTetO, which was synthesized to contain 7 modified TetO elements flanked by two minimal CMV promoter sequences based on pTet-T2 sequences (GenScript) (44). To facilitate selection of clones, a GFP cDNA with the coding region flanked by two LoxP sites was cloned into pBiTetO to generate pBiTetO-GFPLoxP. The *MEG3* cDNA in pCI-MEG3 (16) was modified by replacing AATAAA and its downstream poly(A) tail with a genomic DNA fragment containing the *MEG3* gene polyadenylation signal. The resultant *MEG3* cDNA was then cloned into pBiTetO-GFPLoxP to generate pBiTetO-MEG3-GFPLoxP. To construct pCMV-rtTA3-IRESpuro, a modified tetracycline responsive transactivator (rtTA3) was synthesized with changes in three amino acids including F67S, F86Y, and A209T (16,45) and inserted into pIRESpuro3 (Clontech Laboratories). Plasmids were verified by sequencing.

For stable transfection, U2OS cells were seeded into 6-well cell culture plates and transfected with pBiTetO-MEG3-GFPLoxP and pCMV-rtTA3-IRESpuro at a ratio of 3 to 1 using Mirus TransIT-LT1 according to the manufacture's instructions. Forty-eight hours after transfection, cells were re-seeded in P100 dishes with limited dilution. Approximately ten days after treatment with puromycin (2 µg/mL), drug resistant colonies were isolated using cloning rings. Cells from individual clones were treated with or without doxycycline (1 µg/mL) for 24 h. GFP expression was evaluated under a fluorescence microscope. Cells expressing GFP in Dox-treated wells were further examined for MEG3 expression by qRT-PCR. Two sets of primers were used to detect MEG3. The first set detected a fragment near the 5′ end of the MEG3 cDNA: 5′-ATTAAGCCCTGACCTTTGCTATGC-3′ (forward) and 5′-ATAAGGGTGATGACAGAGTCAGTCG-3′ (reverse); the second set detected the 3′ end of the MEG3: 5′-CTTCAGTGTCTGCATGTGGGAAG-3′ (forward) and 5′-TGCTTTGGAACCGCATCACAG-3′ (reverse). The GAPDH gene was used as an internal reference. The primers for detection of GAPDH were: 5′-GATGACATCAAGAAGGTGGTGAAGC-3′ (forward) and 5′-CGTTGTCATA-CCAGGAAATGAGCTTG-3′ (reverse). Cell clones with suitable MEG3 induction were treated with adenoviruses expressing Cre (Ad-Cre) to remove the floxed GFP. Up to three rounds of virus treatments were needed to completely remove GFP. The removal of GFP was confirmed by qRT-PCR with primer set: 5′-CCACAACGTCTATATCATGGCCG-3′ (forward) and 5′-GTGCTCAGGTAGTGGTTGTCG-3′ (reverse). A total of four clones containing inducible MEG3 were finally obtained and designated as U2OS-MEG3.

Direct stochastic optical reconstruction microscopy (dSTORM)

Fixation

Cells were grown to between 30–90% confluence in chambered coverglass. Cells were rinsed with prewarmed Dulbecco's phosphate-buffered saline with calcium and magnesium (DPBS; Corning) twice using near-simultaneous aspiration and injection of liquid to avoid dehydration. Prewarmed fixation buffer (4% (v/v) paraformaldehyde (Electron Microscopy Sciences), 0.1% (v/v) glutaraldehyde (Electron Microscopy Sciences)) was added and incubated in the dark for 15 min. Fixed cells were rinsed with DPBS. Remaining fixative was quenched with 1% (w/v) sodium borohydride (Sigma-Aldrich) for 7 min. (0.1% is typical, but we have observed better suppression of autofluorescence at 1%.) Cells were further quenched and washed with 50 mM glycine (Bio-Rad) in DPBS (DPBS-G) 3 times for 10 min each. Fixed cells were stored for up to a week in DPBS at 4 °C.

Immunofluorescence

Cells were permeabilized with 0.2% Triton X-100 (*t*-octylphenoxypolyethoxyethanol, Sigma-Aldrich) in DPBS for 10 min and rinsed with DPBS. Cells were blocked with 5% normal donkey serum (EMD Millipore)/0.02% (v/v) Triton X-100 in DPBS for 4 h at room temperature or overnight at 4 °C. Primary antibodies (rabbit anti-p53 [7F5] (Cell Signaling 2527S, Lot 8), mouse anti-Mdm2 [2A10] (Abcam ab16895, Lot GR324625-5)) were applied at 1:1000 and 1:200 dilutions, respectively, in blocking buffer and incubated overnight at 4 °C. Cells were washed with DPBS 6 times for 5 min each. Secondary antibodies (donkey anti-rabbit IgG (Jackson ImmunoResearch) and donkey anti-mouse IgG (Jackson ImmunoResearch)) were labeled as previously described with ATTO 488 (ThermoFisher Scientific) or Alexa Fluor 647 (ThermoFisher Scientific) for a dye ratio of ~1:1 (46). Secondary antibodies were added at 3 µg/mL each in blocking buffer and incubated for 2 h at room temperature in the dark. All subsequent steps were performed in the dark. Cells were washed with DPBS 6 times for 5 min each. Antibody stacks were crosslinked by 4% (v/v) paraformaldehyde in DPBS for 15 min. Remaining fixative was quenched and washed with DPBS-G twice for 5 min each, followed by DPBS twice for 5 min each. Stained cells were stored at 4 °C for up to 2 weeks before imaging.

Combined immunofluorescence and fluorescence in situ hybridization (FISH)

All buffers are RNase-free. Cells were permeabilized with 0.2% Triton X-100 in RNase-free PBS (Corning) for 10 min and rinsed with PBS. No blocking was performed to avoid introducing RNase activity. Primary antibody (rabbit anti-p53, see above) were applied at 1:1000 or 1:200 dilutions, respectively, in PBS and incubated overnight at 4 °C. Cells were washed with PBS 6 times for 5 min each. FISH was performed using buffers and ~20-mer tiled probe sets from Stellaris, according to manufacturer's protocol. In brief, cells were washed with Wash Buffer A 2 times for 3 min. MEG3-Quasar 670 (Stellaris, custom order) or GAPDH-Quasar 570 (Stellaris SMF-2026-1) probe mixture was mixed 1:1000 in Hybridization Buffer and 100 µL was added per well. Steps from this point forward were conducted in the dark. The chambered coverglass was placed in a pre-warmed humidified chamber (large culture dish with damp paper towels) and incubated at 37 °C for 16 h. Cells were washed 2 times for 15 min each with warm Wash Buffer A in the humidified chamber. Secondary antibodies (donkey anti-rabbit conjugated with ATTO 488, see above) were added at 3 µg/mL each in Wash Buffer A and incubated for 1 h at 37 °C in the humidified chamber. Cells were washed 2 times for 2 min each with Wash Buffer B, then 2 times for 5 min each with PBS.

Imaging

Imaging buffer containing 10 mM cysteamine (2-mercaptoethylamine, MEA; Sigma-Aldrich), 3 U/mL pyranose oxidase from *Coriolus* sp. (Sigma P4234), and 90 U/mL catalase was freshly prepared in STORM buffer. Cysteamine stock solution was previously titrated to pH 8 and aliquots frozen. Precipitate in pyranose oxidase/catalase 100x enzyme stock solution was cleared by centrifugation at over 14,000×*g* prior to use. STORM buffer was composed of 10% (w/v) glucose, 10 mM sodium chloride, and 50 mM Tris hydrochloride (pH 8.0). We found the pyranose oxidase buffer (first described in (47)) to be superior to the standard glucose oxidase buffer. This buffer allowed longer imaging times due to minimal pH change, and the enzyme stock lasted several months at 4 °C with no observable decline in imaging quality. 10 mM cysteamine was selected for superior imaging characteristics with different dyes (48). PBS was replaced with the imaging buffer and the slide was mounted on the stage with type F immersion oil (refractive index = 1.515) on a Nikon Ti2 Eclipse inverted microscope. The microscope was equipped with a 100× 1.49 NA APO-TIRF objective with automatic correction collar and a Nikon NSTORM system including 405 nm (20 mW), 488 nm (70 mW), 561 nm (70 mW), and 647 nm (125 mW) lasers, a quadband excitation-emission filter, and a Hamamatsu ORCA Flash4.0 V2 S-CMOS camera. Nikon Elements 5.02 was used for image acquisition. A 10×10 tiled (with 15% overlap) widefield fluorescence image (~790×790 µm^2) was obtained with 1 s exposure using GFPHQ, TexasRedHYQ, or Cy5HYQ filter cubes, from which random individual cells were selected for dSTORM imaging. At least 11000, 256x256 pixel (160 µm/pixel) frames were collected with 10 ms exposure time at 100% laser power with lasers in highly inclined and laminated optical sheet (HILO) configuration (49). Each channel was collected sequentially from longest wavelength to shortest.

Data analysis

Localizations were identified from STORM image stacks using Nikon Elements 5.02 (NSTORM 4.0), with a peak height threshold of 250. Localization lists were exported as tab-delimited text files.

Localization data was processed with custom code written in the freely available Julia scientific computing language (v1.4) (50). Localizations identified in the first 100 frames, while fluorophores are being placed into the "off" state, were excluded. Localizations identified in the last 10 frames were also excluded due to artifacts caused by the change in optical configuration. For each image, a grouping algorithm (SI Algorithm 1; Figure S5) was applied to each channel to combine repeated blinking from single fluorophores and localizations that may be associated (e.g., another fluorophore on same secondary antibody, another secondary antibody on the same primary antibody, another primary antibody on a multimer). The first stage of the grouping algorithm iteratively identified local density maxima by searching a 34.2 nm radius and within a temporal window of 500 frames (5.0 s) of each localization for the localizations with the most neighbors, combining those localizations within the radius of the maxima,

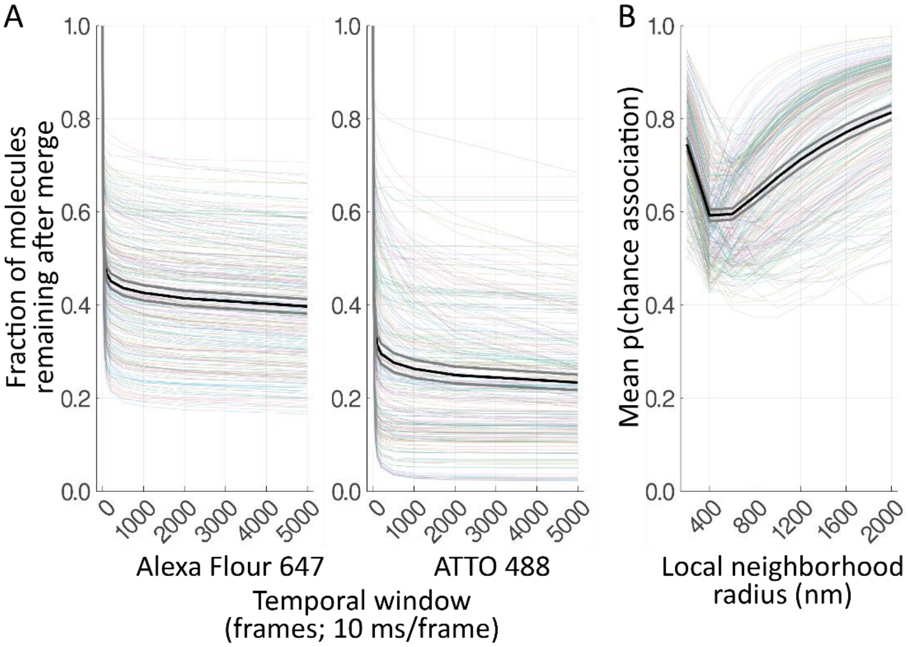

Figure 10. Analysis of algorithm parameters. All cells were repeatedly analyzed with the algorithm during development to characterize the effect of parameter choice on outcome. (A,B) Fraction of molecules remaining after grouping, normalized to the number of molecules with window size 1, as a function of temporal window size (frames, at 10 ms/frame), for Alexa Fluor 647 and ATTO 488. (B) Mean probability of chance association (p(chance association)) as a function of local neighborhood radius (nm). Each faded colored line is from a single cell. Black line shows the mean, gray lines indicate ± 95% confidence interval.

and repeating until all localizations were assigned to a group. The 34.2 nm radius limit was derived from a simulation of the possible orientation and positions of fluorophores in an antibody stack, to account for possible motion of the antibody stack and multiple fluorophores on the stack. The temporal window was applied to account for longer-scale on/off cycles of the fluorophores, as first described for PALM data (43), and was chosen semi-empirically by testing a range of values and selecting the smallest value that merged the most localizations (i.e., where the slope starts to decrease before the plateau) (Figure 10A) and where the merge results appeared suitable (e.g., few temporally separated clusters of localizations were merged).

In the second stage, grouped localizations were merged if they were found within 200 nm of each other by a similar local density maxima search algorithm to further reduce redundancy from autocorrelated localizations. The products of this grouping algorithm were termed “molecules.” The position of the resulting molecule was the mean of its component localizations’ positions, and its linear localization accuracy was the mean of the accuracy for its component localizations divided by the square root of the number of component localizations.

The molecules were paired between channels by an exclusive cross–nearest neighbor algorithm (i.e., closest pair found and then removed, next closest pair found and then removed…; SI Algorithm 3) to obtain a distance distribution between the two sets of molecules. Two analytical approaches were applied, simple and sophisticated. First, the median paired distance was calculated for each cell. Second, a novel approach was developed to control for local density, based on a similar approach applied to single-molecule conventional fluorescence microscopy (29). Random permutations (10,000) of the molecules in the local (800 nm radius) neighborhood around each potential binding pair were generated and the closest pairwise distance in each permutation was calculated to create a Monte Carlo estimation of the distribution of distances due to local density (SI Algorithm 4). The local neighborhood radius of 800 nm was semi-empirically chosen based on testing multiple window sizes with the algorithm and choosing the value that provided a balance of sensitivity (smaller value) and robustness (less inter-sample change as parameter changes) (Figure 10B). The fraction of permutations with a closest distance less than the observed distance was the percentile rank score, indicating the probability of chance association given the local density of both molecule types. Finally, the fraction of pairs within the maximum binding distance (200 nm) and with a probability of chance association of less than 0.1 was calculated for each cell. The maximum binding distance was chosen based on knowledge of the size of the target molecules (up to 20 nm across) and the size of the antibody stacks (up to 70 nm), with allowance for error. Binding fraction for each cell was normalized using a positive and negative control generated from each cell. For the positive control (simulated 100% binding), each putative pair had one member randomly moved to within 80 nm of its partner. For the negative control (simulated 0% binding), all molecules were randomized within 800 nm of their original position, to maintain large-scale structure. For the negative control, between 5 and 30 iterations were conducted, with more iterations when there were fewer molecule pairs to dampen variance, and the median fraction bound of these trials was taken as the zero point.

These data were tested for significance by two-way fixed-factor ANOVA with 2 nested factors (cells within replicates within conditions), with $\alpha = 0.05$, using the SimpleANOVA.jl (v0.6.0) Julia package created by the authors. Data was checked for extreme outliers, heteroscedasticity, and normality of residuals, and were determined to be reasonable. Plots were generated with StatsPlots.jl (v0.14.0) and assembled with Adobe Illustrator (24.0).

Code availability

All the code generated specifically for this manuscript is written in the Julia language and available in the repository at doi: 10.5281/zenodo.3893264. Supporting packages can be obtained within Julia from its public package registry.

Data availability

Raw STORM data files are stored on a local server. STORM localization list text files are available in the repository at doi: 10.5281/zenodo.3892995.

Acknowledgements
We thank Dr. Angie Schmider and Nikon for training on the STORM system; Dr. Hongjae Sunwoo for advice on combining FISH and STORM; Dr. Carolina Eliscovich for help understanding her Monte Carlo-based method; and Dr. Hang Lee of Harvard Catalyst for statistical advice.

Funding and additional information
RJS: R01CA193520, R01DK062472, S10RR027931; NCB: T32DK007540; AK and YZ: R01CA193520; and The Jarislowsky Foundation. The content is solely the responsibility of the authors and does not necessarily represent the official views of the National Institutes of Health.

Conflict of Interest: The authors declare no conflicts of interest in regards to this manuscript.

References

1. Zhang, X., Zhou, Y., Mehta, K. R., Danila, D. C., Scolavino, S., Johnson, S. R., and Klibanski, A. (2003) A pituitary-derived MEG3 isoform functions as a growth suppressor in tumor cells. *J Clin Endocrinol Metab* **88**, 5119-5126
2. Naoki, M., Hirotaka, W., Shigeharu, W., Toshihiko, S., Masashi, N., Kohzoh, A., Takashi, K., Azim, S. M., Tomoko, K. I., and Fumitoshi, I. (2000) Identification of an imprinted gene, *Meg3*/*Gtl2* and its human homologue *MEG3*, first mapped on mouse distal chromosome 12 and human chromosome 14q. *Genes Cells* **5**, 211-220
3. Li, R., Fang, L., Pu, Q., Bu, H., Zhu, P., Chen, Z., Yu, M., Li, X., Weiland, T., Bansal, A., Ye, S. Q., Wei, Y., Jiang, J., and Wu, M. (2018) MEG3-4 is a miRNA decoy that regulates IL-1β abundance to initiate and then limit inflammation to prevent sepsis during lung infection. *Sci Signal* **11**
4. Mondal, T., Subhash, S., Vaid, R., Enroth, S., Uday, S., Reinius, B., Mitra, S., Mohammed, A., James, A. R., Hoberg, E., Moustakas, A., Gyllensten, U., Jones, S. J., Gustafsson, C. M., Sims, A. H., Westerlund, F., Gorab, E., and Kanduri, C. (2015) MEG3 long noncoding RNA regulates the TGF-beta pathway genes through formation of RNA-DNA triplex structures. *Nat Commun* **6**, 7743
5. Cheunsuchon, P., Zhou, Y., Zhang, X., Lee, H., Chen, W., Nakayama, Y., Rice, K. A., Tessa Hedley-Whyte, E., Swearingen, B., and Klibanski, A. (2011) Silencing of the imprinted *DLK1-MEG3* locus in human clinically nonfunctioning pituitary adenomas. *Am J Pathol* **179**, 2120-2130
6. Gejman, R., Batista, D. L., Zhong, Y., Zhou, Y., Zhang, X., Swearingen, B., Stratakis, C. A., Hedley-Whyte, E. T., and Klibanski, A. D. (2008) Selective loss of MEG3 expression and intergenic differentially methylated region hypermethylation in the MEG3/DLK1 locus in human clinically nonfunctioning pituitary adenomas. *J Clin Endocrinol Metab* **93**, 4119-4125
7. Zhao, J., Dahle, D., Zhou, Y., Zhang, X., and Klibanski, A. D. (2005) Hypermethylation of the promoter region is associated with the loss of MEG3 gene expression in human pituitary tumors. *J Clin Endocrinol Metab* **90**, 2179-2186
8. Zhang, X., Gejman, R., Mahta, A., Zhong, Y., Rice, K. A., Zhou, Y., Cheunsuchon, P., Louis, D. N., and Klibanski, A. D. (2010) Maternally expressed gene 3, an imprinted noncoding RNA gene, is associated with meningioma pathogenesis and progression. *Cancer Res* **70**, 2350-2358
9. Sheng, X., Li, J., Yang, L., Chen, Z., Zhao, Q., Tan, L., Zhou, Y., and Li, J. D. (2014) Promoter hypermethylation influences the suppressive role of maternally expressed 3, a long non-coding RNA, in the development of epithelial ovarian cancer. *Oncol Rep* **32**, 277-285
10. Jia, L. F., Wei, S. B., Gan, Y. H., Guo, Y., Gong, K., Mitchelson, K., Cheng, J., and Yu, G. Y. (2014) Expression, regulation and roles of miR-26a and MEG3 in tongue squamous cell carcinoma. *Int J Cancer* **135**, 2282-2293
11. Lu, K. H., Li, W., Liu, X. H., Sun, M., Zhang, M. L., Wu, W. Q., Xie, W. P., and Hou, Y. D. (2013) Long non-coding RNA MEG3 inhibits NSCLC cells proliferation and induces apoptosis by affecting p53 expression. *BMC Cancer* **13**, 461

12. Qu, C., Jiang, T., Li, Y., Wang, X., Cao, H., Xu, H., Qu, J., and Chen, J. G. (2013) Gene expression and IG-DMR hypomethylation of maternally expressed gene 3 in developing corticospinal neurons. *Gene Expr Patterns* **13**, 51-56
13. Sun, M., Xia, R., Jin, F., Xu, T., Liu, Z., De, W., and Liu, X. D. (2014) Downregulated long noncoding RNA MEG3 is associated with poor prognosis and promotes cell proliferation in gastric cancer. *Tumour Biol* **35**, 1065-1073
14. Huang, L., Yan, Z., Liao, X., Li, Y., Yang, J., Wang, Z. G., Zuo, Y., Kawai, H., Shadfan, M., Ganapathy, S., and Yuan, Z. M. (2011) The p53 inhibitors MDM2/MDMX complex is required for control of p53 activity in vivo. *Proc Natl Acad Sci U S A* **108**, 12001-12006
15. Linares, L. K., Hengstermann, A., Ciechanover, A., Muller, S., and Scheffner, M. (2003) HdmX stimulates Hdm2-mediated ubiquitination and degradation of p53. *Proc Natl Acad Sci U S A* **100**, 12009-12014
16. Zhou, Y., Zhong, Y., Wang, Y., Zhang, X., Batista, D. L., Gejman, R., Ansell, P. J., Zhao, J., Weng, C., and Klibanski, A. D. (2007) Activation of p53 by MEG3 non-coding RNA. *J Biol Chem* **282**, 24731-24742
17. Ryan, K. M., Phillips, A. C., and Vousden, K. H. (2001) Regulation and function of the p53 tumor suppressor protein. *Curr Opin Cell Biol* **13**, 332-337
18. Perry, M. E. (2010) The regulation of the p53-mediated stress response by MDM2 and MDM4. *Cold Spring Harb Perspect Biol* **2**, a000968
19. Toledo, F., and Wahl, G. M. (2006) Regulating the p53 pathway: in vitro hypotheses, in vivo veritas. *Nat Rev Cancer* **6**, 909-923
20. Gu, J., Kawai, H., Nie, L., Kitao, H., Wiederschain, D., Jochemsen, A. G., Parant, J., Lozano, G., and Yuan, Z. M. (2002) Mutual dependence of MDM2 and MDMX in their functional inactivation of p53. *J Biol Chem* **277**, 19251-19254
21. Bauer, N. C., Doetsch, P. W., and Corbett, A. H. (2015) Mechanisms regulating protein localization. *Traffic* **16**, 1039-1061
22. Zheng, H., You, H., Zhou, X. Z., Murray, S. A., Uchida, T., Wulf, G., Gu, L., Tang, X., Lu, K. P., and Xiao, Z. X. (2002) The prolyl isomerase Pin1 is a regulator of p53 in genotoxic response. *Nature* **419**, 849-853
23. Zacchi, P., Gostissa, M., Uchida, T., Salvagno, C., Avolio, F., Volinia, S., Ronai, Z., Blandino, G., Schneider, C., and Del Sal, G. (2002) The prolyl isomerase Pin1 reveals a mechanism to control p53 functions after genotoxic insults. *Nature* **419**, 853-857
24. Zhu, J., Liu, S., Ye, F., Shen, Y., Tie, Y., Zhu, J., Wei, L., Jin, Y., Fu, H., Wu, Y., and Zheng, X. D. (2015) Long noncoding RNA MEG3 interacts with p53 protein and regulates partial p53 target genes in hepatoma cells. *PLoS One* **10**, e0139790
25. Yan, H., Yuan, J., Gao, L., Rao, J., and Hu, J. (2016) Long noncoding RNA MEG3 activation of p53 mediates ischemic neuronal death in stroke. *Neuroscience* **337**, 191-199
26. Feher, K., Halstead, J. M., Goyette, J., and Gaus, K. (2019) Can single molecule localization microscopy detect nanoclusters in T cells? *Curr Opin Chem Biol* **51**, 130-137
27. Pageon, S. V., Nicovich, P. R., Mollazade, M., Tabarin, T., and Gaus, K. (2016) Clus-DoC: a combined cluster detection and colocalization analysis for single-molecule localization microscopy data. *Mol Biol Cell* **27**, 3627-3636
28. Levet, F., Julien, G., Galland, R., Butler, C., Beghin, A., Chazeau, A., Hoess, P., Ries, J., Giannone, G., and Sibarita, J. B. (2019) A tessellation-based colocalization analysis approach for single-molecule localization microscopy. *Nat Commun* **10**, 2379
29. Eliscovich, C., Shenoy, S. M., and Singer, R. H. (2017) Imaging mRNA and protein interactions within neurons. *Proc Natl Acad Sci U S A* **114**, E1875-e1884
30. Riley, K. J., and Maher, L. J., 3rd. (2007) p53 RNA interactions: new clues in an old mystery. *RNA* **13**, 1825-1833

31. Vassilev, L. T., Vu, B. T., Graves, B., Carvajal, D., Podlaski, F., Filipovic, Z., Kong, N., Kammlott, U., Lukacs, C., Klein, C., Fotouhi, N., and Liu, E. A. (2004) In vivo activation of the p53 pathway by small-molecule antagonists of MDM2. *Science* **303**, 844-848
32. Zhao, J., Ohsumi, T. K., Kung, J. T., Ogawa, Y., Grau, D. J., Sarma, K., Song, J. J., Kingston, R. E., Borowsky, M., and Lee, J. T. (2010) Genome-wide identification of polycomb-associated RNAs by RIP-seq. *Mol Cell* **40**, 939-953
33. Kaneko, S., Bonasio, R., Saldana-Meyer, R., Yoshida, T., Son, J., Nishino, K., Umezawa, A., and Reinberg, D. (2014) Interactions between JARID2 and noncoding RNAs regulate PRC2 recruitment to chromatin. *Mol Cell* **53**, 290-300
34. Das, P. P., Hendrix, D. A., Apostolou, E., Buchner, A. H., Canver, M. C., Beyaz, S., Ljuboja, D., Kuintzle, R., Kim, W., Karnik, R., Shao, Z., Xie, H., Xu, J., De Los Angeles, A., Zhang, Y., Choe, J., Jun, D. L., Shen, X., Gregory, R. I., Daley, G. Q., Meissner, A., Kellis, M., Hochedlinger, K., Kim, J., and Orkin, S. H. (2015) PRC2 is required to maintain expression of the maternal *Gtl2-Rian-Mirg* locus by preventing de novo DNA methylation in mouse embryonic stem cells. *Cell Rep* **12**, 1456-1470
35. Uroda, T., Anastasakou, E., Rossi, A., Teulon, J. M., Pellequer, J. L., Annibale, P., Pessey, O., Inga, A., Chillon, I., and Marcia, M. (2019) Conserved pseudoknots in lncRNA MEG3 are essential for stimulation of the p53 pathway. *Mol Cell* **75**, 982-995.e989
36. Savchenko, A., Yurchenko, M., Snopok, B., and Kashuba, E. (2008) Study on the spatial architecture of p53, MDM2, and p14ARF containing complexes. *Mol Biotechnol* **41**, 270
37. Li, L., Tao, Q., Jin, H., van Hasselt, A., Poon, F. F., Wang, X., Zeng, M.-S., Jia, W.-H., Zeng, Y.-X., Chan, A. T. C., and Cao, Y. (2010) The tumor zuppressor UCHL1 forms a complex with p53/MDM2/ARF to promote p53 signaling and is frequently silenced in nasopharyngeal carcinoma. *Clinical Cancer Research* **16**, 2949-2958
38. Sloan, K. E., Bohnsack, M. T., and Watkins, N. J. (2013) The 5S RNP couples p53 homeostasis to ribosome biogenesis and nucleolar stress. *Cell Rep* **5**, 237-247
39. Saphire, E. O., Stanfield, R. L., Crispin, M. D., Parren, P. W., Rudd, P. M., Dwek, R. A., Burton, D. R., and Wilson, I. A. (2002) Contrasting IgG structures reveal extreme asymmetry and flexibility. *J Mol Biol* **319**, 9-18
40. Sograte-Idrissi, S., Oleksiievets, N., Isbaner, S., Eggert-Martinez, M., Enderlein, J., Tsukanov, R., and Opazo, F. (2019) Nanobody detection of standard fluorescent proteins enables multi-target DNA-PAINT with high resolution and minimal displacement errors. *Cells* **8**
41. Carrington, G., Tomlinson, D., and Peckham, M. (2019) Exploiting nanobodies and affimers for superresolution imaging in light microscopy. *Mol Biol Cell* **30**, 2737-2740
42. Ingram, J. R., Schmidt, F. I., and Ploegh, H. L. (2018) Exploiting Nanobodies' Singular Traits. *Annu Rev Immunol* **36**, 695-715
43. Annibale, P., Vanni, S., Scarselli, M., Rothlisberger, U., and Radenovic, A. (2011) Identification of clustering artifacts in photoactivated localization microscopy. *Nat Methods* **8**, 527
44. Loew, R., Heinz, N., Hampf, M., Bujard, H., and Gossen, M. (2010) Improved Tet-responsive promoters with minimized background expression. *BMC Biotechnol* **10**, 81
45. Das, A. T., Zhou, X., Vink, M., Klaver, B., Verhoef, K., Marzio, G., and Berkhout, B. (2004) Viral evolution as a tool to improve the tetracycline-regulated gene expression system. *J Biol Chem* **279**, 18776-18782
46. Schmider, A. B., Vaught, M., Bauer, N. C., Elliott, H. L., Godin, M. D., Ellis, G. E., Nigrovic, P. A., and Soberman, R. J. (2019) The organization of leukotriene biosynthesis on the nuclear envelope revealed by single molecule localization microscopy and computational analyses. *PLoS One* **14**, e0211943
47. Swoboda, M., Henig, J., Cheng, H. M., Brugger, D., Haltrich, D., Plumere, N., and Schlierf, M. (2012) Enzymatic oxygen scavenging for photostability without pH drop in single-molecule experiments. *ACS Nano* **6**, 6364-6369

48. van de Linde, S., Loschberger, A., Klein, T., Heidbreder, M., Wolter, S., Heilemann, M., and Sauer, M. (2011) Direct stochastic optical reconstruction microscopy with standard fluorescent probes. *Nat Protoc* **6**, 991-1009
49. Tokunaga, M., Imamoto, N., and Sakata-Sogawa, K. (2008) Highly inclined thin illumination enables clear single-molecule imaging in cells. *Nat Methods* **5**, 159-161
50. Bezanson, J., Edelman, A., Karpinski, S., and Shah, V. B. (2017) Julia: a fresh approach to numerical computing. *SIAM Review* **59**, 65-98
51. Rose, A. S., Bradley, A. R., Valasatava, Y., Duarte, J. M., Prlić, A., and Rose, P. W. (2018) NGL viewer: web-based molecular graphics for large complexes. *Bioinformatics* **34**, 3755-3758